

Characterizing the localized surface plasmon resonance behaviors of Au nanorings and tracking their diffusion in bio-tissue with optical coherence tomography

Cheng-Kuang Lee,¹ Hung-Yu Tseng,¹ Chia-Yun Lee,² Shou-Yen Wu,¹ Ting-Ta Chi,¹
Kai-Min Yang,¹ Han-Yi Elizabeth Chou,² Meng-Tsan Tsai,³ Jyh-Yang Wang,¹
Yean-Woei Kiang,¹ Chun-Pin Chiang,² and C. C. Yang^{1,*}

¹*Institute of Photonics and Optoelectronics, National Taiwan University, 1,
Roosevelt Road, Section 4, Taipei, 10617, Taiwan*

²*Graduate Institute of Oral Biology, National Taiwan University, 1, Changde St., Taipei, 10002, Taiwan*

³*Department of Electrical Engineering, Chang Gung University, 259,
Wen-Hwa 1st Road, Kwei-Shan, Tao-Yuan, 33302, Taiwan*

*ccy@cc.ee.ntu.edu.tw

Abstract: The characterization results of the localized surface plasmon resonance (LSPR) of Au nanorings (NRs) with optical coherence tomography (OCT) are first demonstrated. Then, the diffusion behaviors of Au NRs in mouse liver samples tracked with OCT are shown. For such research, aqueous solutions of Au NRs with two different localized surface plasmon resonance (LSPR) wavelengths are prepared and characterized. Their LSPR-induced extinction cross sections at 1310 nm are estimated with OCT scanning of solution droplets on coverslip to show reasonably consistent results with the data at individual LSPR wavelengths and at 1310 nm obtained from transmission measurements of Au NR solutions and numerical simulations. The resonant and non-resonant Au NRs are delivered into mouse liver samples for tracking Au NR diffusion in the samples through continuous OCT scanning for one hour. With resonant Au NRs, the average A-mode scan profiles of OCT scanning at different delay times clearly demonstrate the extension of strong backscattering depth with time. The calculation of speckle variance among successive OCT scanning images, which is related to the local transport speed of Au NRs, leads to the illustrations of downward propagation and spreading of major Au NR motion spot with time.

©2010 Optical Society of America

OCIS codes: (110.4500) Optical coherence tomography; (240.6680) Surface plasmons.

References and links

1. D. C. Adler, S. W. Huang, R. Huber, and J. G. Fujimoto, "Photothermal detection of gold nanoparticles using phase-sensitive optical coherence tomography," *Opt. Express* **16**(7), 4376–4393 (2008), <http://www.opticsinfobase.org/oe/abstract.cfm?uri=oe-16-7-4376>.
2. C. Zhou, T. H. Tsai, D. C. Adler, H. C. Lee, D. W. Cohen, A. Mondelblatt, Y. Wang, J. L. Connolly, and J. G. Fujimoto, "Photothermal optical coherence tomography in ex vivo human breast tissues using gold nanoshells," *Opt. Lett.* **35**(5), 700–702 (2010).
3. M. C. Skala, M. J. Crow, A. Wax, and J. A. Izatt, "Photothermal optical coherence tomography of epidermal growth factor receptor in live cells using immunotargeted gold nanospheres," *Nano Lett.* **8**(10), 3461–3467 (2008).
4. C. S. Kim, P. Wilder-Smith, Y. C. Ahn, L. H. L. Liaw, Z. Chen, and Y. J. Kwon, "Enhanced detection of early-stage oral cancer in vivo by optical coherence tomography using multimodal delivery of gold nanoparticles," *J. Biomed. Opt.* **14**(3), 034008 (2009).
5. J. Chen, F. Saeki, B. J. Wiley, H. Cang, M. J. Cobb, Z. Y. Li, L. Au, H. Zhang, M. B. Kimmey, X. Li, and Y. Xia, "Gold nanocages: bioconjugation and their potential use as optical imaging contrast agents," *Nano Lett.* **5**(3), 473–477 (2005).

6. H. Cang, T. Sun, Z. Y. Li, J. Chen, B. J. Wiley, Y. Xia, and X. Li, "Gold nanocages as contrast agents for spectroscopic optical coherence tomography," *Opt. Lett.* **30**(22), 3048–3050 (2005).
7. E. V. Zagaynova, M. V. Shirmanova, M. Y. Kirillin, B. N. Khlebtsov, A. G. Orlova, I. V. Balalaeva, M. A. Sirotkina, M. L. Bugrova, P. D. Agrba, and V. A. Kamensky, "Contrasting properties of gold nanoparticles for optical coherence tomography: phantom, in vivo studies and Monte Carlo simulation," *Phys. Med. Biol.* **53**(18), 4995–5009 (2008).
8. M. Kirillin, M. Shirmanova, M. Sirotkina, M. Bugrova, B. Khlebtsov, and E. Zagaynova, "Contrasting properties of gold nanoshells and titanium dioxide nanoparticles for optical coherence tomography imaging of skin: Monte Carlo simulations and in vivo study," *J. Biomed. Opt.* **14**(2), 021017 (2009).
9. A. M. Gobin, M. H. Lee, N. J. Halas, W. D. James, R. A. Drezek, and J. L. West, "Near-infrared resonant nanoshells for combined optical imaging and photothermal cancer therapy," *Nano Lett.* **7**(7), 1929–1934 (2007).
10. A. L. Oldenburg, M. N. Hansen, D. A. Zweifel, A. Wei, and S. A. Boppart, "Plasmon-resonant gold nanorods as low backscattering albedo contrast agents for optical coherence tomography," *Opt. Express* **14**(15), 6724–6738 (2006), <http://www.opticsinfobase.org/abstract.cfm?URI=oe-14-15-6724>.
11. D. P. O'Neal, L. R. Hirsch, N. J. Halas, J. D. Payne, and J. L. West, "Photo-thermal tumor ablation in mice using near infrared-absorbing nanoparticles," *Cancer Lett.* **209**(2), 171–176 (2004).
12. C. Loo, A. Lowery, N. Halas, J. West, and R. Drezek, "Immunotargeted nanoshells for integrated cancer imaging and therapy," *Nano Lett.* **5**(4), 709–711 (2005).
13. B. Khlebtsov, V. Zharov, A. Melnikov, V. Tuchin, and N. Khlebtsov, "Optical amplification of photothermal therapy with gold nanoparticles and nanoclusters," *Nanotechnology* **17**(20), 5167–5179 (2006).
14. I. H. El-Sayed, X. Huang, and M. A. El-Sayed, "Selective laser photo-thermal therapy of epithelial carcinoma using anti-EGFR antibody conjugated gold nanoparticles," *Cancer Lett.* **239**(1), 129–135 (2006).
15. V. P. Zharov, K. E. Mercer, E. N. Galitovskaya, and M. S. Smeltzer, "Photothermal nanotherapeutics and nanodiagnosics for selective killing of bacteria targeted with gold nanoparticles," *Biophys. J.* **90**(2), 619–627 (2006).
16. X. Ji, R. Shao, A. M. Elliott, R. J. Stafford, E. Esparza-Coss, J. A. Bankson, G. Liang, Z.-P. Luo, K. Park, J. T. Markert, and C. Li, "Bifunctional Gold Nanoshells with a Superparamagnetic Iron Oxide-Silica Core Suitable for Both MR Imaging and Photothermal Therapy," *Nano Lett.* **11**(17), 6245–6251 (2007).
17. F. Gu, R. Karnik, A. Wang, F. Alexis, E. Levynissenbaum, S. Hong, R. Langer, and O. Farokhzad, "Targeted nanoparticles for cancer therapy," *Nano Today* **2**(3), 14–21 (2007).
18. S. J. Son, X. Bai, and S. B. Lee, "Inorganic hollow nanoparticles and nanotubes in nanomedicine Part 2: Imaging, diagnostic, and therapeutic applications," *Drug Discov. Today* **12**(15-16), 657–663 (2007).
19. L. Au, D. Zheng, F. Zhou, Z. Y. Li, X. Li, and Y. Xia, "A quantitative study on the photothermal effect of immuno gold nanocages targeted to breast cancer cells," *ACS Nano* **2**(8), 1645–1652 (2008).
20. X. Huang, P. K. Jain, I. H. El-Sayed, and M. A. El-Sayed, "Plasmonic photothermal therapy (PPTT) using gold nanoparticles," *Lasers Med. Sci.* **23**(3), 217–228 (2008).
21. P. K. Jain, I. H. El-Sayed, and M. A. El-Sayed, "Au nanoparticles target cancer," *nano today* **2**, 18–29 (2008).
22. E. B. Dickerson, E. C. Dreaden, X. Huang, I. H. El-Sayed, H. Chu, S. Pushpanketh, J. F. McDonald, and M. A. El-Sayed, "Gold nanorod assisted near-infrared plasmonic photothermal therapy (PPTT) of squamous cell carcinoma in mice," *Cancer Lett.* **269**(1), 57–66 (2008).
23. J. L. Li, L. Wang, X. Y. Liu, Z. P. Zhang, H. C. Guo, W. M. Liu, and S. H. Tang, "In vitro cancer cell imaging and therapy using transferrin-conjugated gold nanoparticles," *Cancer Lett.* **274**(2), 319–326 (2009).
24. P. Cherukuri, E. S. Glazer, and S. A. Curley, "Targeted hyperthermia using metal nanoparticles," *Adv. Drug Deliv. Rev.* **62**(3), 339–345 (2010).
25. X. Huang, and M. A. El-Sayed, "Gold nanoparticles: Optical properties and implementations in cancer diagnosis and photothermal therapy," *J. Advert. Res.* **1**(1), 13–28 (2010).
26. T. Yamada, Y. Iwasaki, H. Tada, H. Iwabuki, M. K. Chuah, T. VandenDriessche, H. Fukuda, A. Kondo, M. Ueda, M. Seno, K. Tanizawa, and S. Kuroda, "Nanoparticles for the delivery of genes and drugs to human hepatocytes," *Nat. Biotechnol.* **21**(8), 885–890 (2003).
27. P. Ghosh, G. Han, M. De, C. K. Kim, and V. M. Rotello, "Gold nanoparticles in delivery applications," *Adv. Drug Deliv. Rev.* **60**(11), 1307–1315 (2008).
28. A. H. Faraji, and P. Wipf, "Nanoparticles in cellular drug delivery," *Bioorg. Med. Chem.* **17**(8), 2950–2962 (2009).
29. D. Pissuwan, T. Niidome, and M. B. Cortie, "*The forthcoming applications of gold nanoparticles in drug and gene delivery systems.*" *Journal of Controlled Release* Available online 11 December 2009.
30. A. G. Tkachenko, H. Xie, Y. Liu, D. Coleman, J. Ryan, W. R. Glomm, M. K. Shipton, S. Franzen, and D. L. Feldheim, "Cellular trajectories of peptide-modified gold particle complexes: comparison of nuclear localization signals and peptide transduction domains," *Bioconjug. Chem.* **15**(3), 482–490 (2004).
31. P. H. Yang, X. Sun, J. F. Chiu, H. Sun, and Q. Y. He, "Transferrin-mediated gold nanoparticle cellular uptake," *Bioconjug. Chem.* **16**(3), 494–496 (2005).
32. J. A. Ryan, K. W. Overton, M. E. Speight, C. N. Oldenburg, L. N. Loo, W. Robarge, S. Franzen, and D. L. Feldheim, "Cellular uptake of gold nanoparticles passivated with BSA-SV40 large T antigen conjugates," *Anal. Chem.* **79**(23), 9150–9159 (2007).
33. B. D. Chithrani, and W. C. W. Chan, "Elucidating the mechanism of cellular uptake and removal of protein-coated gold nanoparticles of different sizes and shapes," *Nano Lett.* **7**(6), 1542–1550 (2007).
34. T. S. Hauck, A. A. Ghazani, and W. C. W. Chan, "Assessing the effect of surface chemistry on gold nanorod uptake, toxicity, and gene expression in mammalian cells," *Small* **4**(1), 153–159 (2008).

35. J. L. Li, L. Wang, X. Y. Liu, Z. P. Zhang, H. C. Guo, W. M. Liu, and S. H. Tang, "In vitro cancer cell imaging and therapy using transferrin-conjugated gold nanoparticles," *Cancer Lett.* **274**(2), 319–326 (2009).
36. X. H. N. Xu, J. Chen, R. B. Jeffers, and S. V. Kyriacou, "Direct Measurement of Sizes and Dynamics of Single Living Membrane Transporters Using Nano-Optics," *Nano Lett.* **2**(3), 175–182 (2002).
37. J. P. Richard, K. Melikov, E. Vives, C. Ramos, B. Verbeure, M. J. Gait, L. V. Chernomordik, and B. Lebleu, "Cell-penetrating peptides. A reevaluation of the mechanism of cellular uptake," *J. Biol. Chem.* **278**(1), 585–590 (2002).
38. X. H. N. Xu, W. J. Brownlow, S. V. Kyriacou, Q. Wan, and J. J. Viola, "Real-time probing of membrane transport in living microbial cells using single nanoparticle optics and living cell imaging," *Biochemistry* **43**(32), 10400–10413 (2004).
39. B. D. Chithrani, A. A. Ghazani, and W. C. W. Chan, "Determining the size and shape dependence of gold nanoparticle uptake into mammalian cells," *Nano Lett.* **6**(4), 662–668 (2006).
40. D. A. Giljohann, D. S. Seferos, P. C. Patel, J. E. Millstone, N. L. Rosi, and C. A. Mirkin, "Oligonucleotide loading determines cellular uptake of DNA-modified gold nanoparticles," *Nano Lett.* **7**(12), 3818–3821 (2007).
41. K. J. Lee, P. D. Nallathambi, L. M. Browning, C. J. Osgood, and X. H. N. Xu, "In vivo imaging of transport and biocompatibility of single silver nanoparticles in early development of zebrafish embryos," *ACS Nano* **1**(2), 133–143 (2007).
42. T. B. Huff, M. N. Hansen, Y. Zhao, J. X. Cheng, and A. Wei, "Controlling the cellular uptake of gold nanorods," *Langmuir* **23**(4), 1596–1599 (2007).
43. Z. J. Zhu, P. S. Ghosh, O. R. Miranda, R. W. Vachet, and V. M. Rotello, "Multiplexed screening of cellular uptake of gold nanoparticles using laser desorption/ionization mass spectrometry," *J. Am. Chem. Soc.* **130**(43), 14139–14143 (2008).
44. D. B. Chithrani, M. Dunne, J. Stewart, C. Allen, and D. A. Jaffray, "Cellular uptake and transport of gold nanoparticles incorporated in a liposomal carrier," *Nanomedicine* **6**(1), 161–169 (2010).
45. M. C. Daniel, and D. Astruc, "Gold nanoparticles: assembly, supramolecular chemistry, quantum-size-related properties, and applications toward biology, catalysis, and nanotechnology," *Chem. Rev.* **104**(1), 293–346 (2004).
46. C. Loo, A. Lin, L. Hirsch, M. H. Lee, J. Barton, N. Halas, J. West, and R. Drezek, "Nanoshell-enabled photonics-based imaging and therapy of cancer," *Technol. Cancer Res. Treat.* **3**(1), 33–40 (2004).
47. A. W. H. Lin, N. A. Lewinski, J. L. West, N. J. Halas, and R. A. Drezek, "Optically tunable nanoparticle contrast agents for early cancer detection: model-based analysis of gold nanoshells," *J. Biomed. Opt.* **10**(6), 064035 (2005).
48. T. S. Troutman, J. K. Barton, and M. Romanowski, "Biodegradable Plasmon Resonant Nanoshells," *Adv. Mater. (Deerfield Beach Fla.)* **20**(13), 2604–2608 (2008).
49. J. Gao, C. M. Bender, and C. J. Murphy, "Dependence of the Gold Nanorod Aspect Ratio on the Nature of the Directing Surfactant in Aqueous Solution," *Langmuir* **19**(21), 9065–9070 (2003).
50. J. Pérez-Juste, L. M. Liz-Marzán, S. Carnie, D. Y. C. Chan, and P. Mulvaney, "Electric Field Directed Growth of Gold Nanorods in Aqueous Surfactant Solutions," *Adv. Funct. Mater.* **14**(6), 571–579 (2004).
51. C. J. Murphy, T. K. Sau, A. M. Gole, C. J. Orendorff, J. Gao, L. Gou, S. E. Hunyadi, and T. Li, "Anisotropic metal nanoparticles: Synthesis, assembly, and optical applications," *J. Phys. Chem. B* **109**(29), 13857–13870 (2005).
52. T. S. Troutman, J. K. Barton, and M. Romanowski, "Optical coherence tomography with plasmon resonant nanorods of gold," *Opt. Lett.* **32**(11), 1438–1440 (2007).
53. J. Chen, B. Wiley, Z. Y. Li, D. Campbell, F. Saeki, H. Cang, L. Au, J. Lee, X. Li, and Y. Xia, "Gold Nanocages: Engineering Their Structure for Biomedical Applications," *Adv. Mater. (Deerfield Beach Fla.)* **17**(18), 2255–2261 (2005).
54. J. Chen, D. Wang, J. Xi, L. Au, A. Siekkinen, A. Warsen, Z. Y. Li, H. Zhang, Y. Xia, and X. Li, "Immuno gold nanocages with tailored optical properties for targeted photothermal destruction of cancer cells," *Nano Lett.* **7**(5), 1318–1322 (2007).
55. E. E. Connor, J. Mwamuka, A. Gole, C. J. Murphy, and M. D. Wyatt, "Gold nanoparticles are taken up by human cells but do not cause acute cytotoxicity," *Small* **1**(3), 325–327 (2005).
56. S. J. Oldenburg, R. D. Averitt, S. L. Westcott, and N. J. Halas, "Nanoengineering of optical resonances," *Chem. Phys. Lett.* **288**(2-4), 243–247 (1998).
57. V. Sharma, K. Park, and M. Srinivasarao, "Shape separation of gold nanorods using centrifugation," *Proc. Natl. Acad. Sci. U.S.A.* **106**(13), 4981–4985 (2009).
58. J. Aizpurua, P. Hanarp, D. S. Sutherland, M. Käll, G. W. Bryant, and F. J. García de Abajo, "Optical properties of gold nanorings," *Phys. Rev. Lett.* **90**(5), 057401 (2003).
59. E. M. Larsson, J. Alegret, M. Käll, and D. S. Sutherland, "Sensing characteristics of NIR localized surface plasmon resonances in gold nanorings for application as ultrasensitive biosensors," *Nano Lett.* **7**(5), 1256–1263 (2007).
60. F. Hao, E. M. Larsson, T. A. Ali, D. S. Sutherland, and P. Nordlander, "Shedding Light on Dark Plasmons in Gold Nanorings," *Chem. Phys. Lett.* **458**(4-6), 262–266 (2008).
61. D. Huang, E. A. Swanson, C. P. Lin, J. S. Schuman, W. G. Stinson, W. Chang, M. R. Hee, T. Flotte, K. Gregory, C. A. Puliafito, and J. G. Fujimoto, "Optical coherence tomography," *Science* **254**(5035), 1178–1181 (1991).
62. M. A. Sirotkina, M. V. Shirmanova, M. L. Bugrova, V. V. Elagin, P. A. Agrba, M. Yu. Kirillin, V. A. Kamensky, and E. V. Zagaynova, "Continuous optical coherence tomography monitoring of nanoparticles accumulation in biological tissues," *J. Nanopart. Res.* (2010). <http://www.springerlink.com/content/f038744m089132jq/>

63. C. C. Yang, M.-T. Tsai, H.-C. Lee, C.-K. Lee, C.-H. Yu, H.-M. Chen, C.-P. Chiang, C.-C. Chang, Y.-M. Wang, and C. C. Yang, "Effective indicators for diagnosis of oral cancer using optical coherence tomography," *Opt. Express* **16**(20), 15847–15862 (2008), <http://www.opticsinfobase.org/oe/abstract.cfm?uri=oe-16-20-15847>.
64. M. T. Tsai, C. K. Lee, H. C. Lee, H. M. Chen, C. P. Chiang, Y. M. Wang, and C. C. Yang, "Differentiating oral lesions in different carcinogenesis stages with optical coherence tomography," *J. Biomed. Opt.* **14**(4), 044028 (2009).
65. C. K. Lee, M. T. Tsai, H. C. Lee, H. M. Chen, C. P. Chiang, Y. M. Wang, and C. C. Yang, "Diagnosis of oral submucous fibrosis with optical coherence tomography," *J. Biomed. Opt.* **14**(5), 054008 (2009).
66. A. Mariampillai, B. A. Standish, E. H. Moriyama, M. Khurana, N. R. Munce, M. K. K. Leung, J. Jiang, A. Cable, B. C. Wilson, I. A. Vitkin, and V. X. D. Yang, "Speckle variance detection of microvasculature using swept-source optical coherence tomography," *Opt. Lett.* **33**(13), 1530–1532 (2008).
67. A. Mariampillai, M. K. K. Leung, M. Jarvi, B. A. Standish, K. Lee, B. C. Wilson, A. Vitkin, and V. X. D. Yang, "Optimized speckle variance OCT imaging of microvasculature," *Opt. Lett.* **35**(8), 1257–1259 (2010).
68. H. Y. Tseng, C. K. Lee, S. Y. Wu, T. T. Chi, K. M. Yang, J. Y. Wang, Y. W. Kiang, C. C. Yang, M. T. Tsai, Y. C. Wu, H. Y. E. Chou, and C. P. Chiang, "Au nanorings for enhancing absorption and backscattering monitored with optical coherence tomography," *Nanotechnology* **21**(29), 295102 (2010).
69. D. J. Faber, F. J. van der Meer, M. C. G. Aalders, and T. G. van Leeuwen, "Quantitative measurement of attenuation coefficients of weakly scattering media using optical coherence tomography," *Opt. Express* **12**(19), 4353–4365 (2004), <http://www.opticsinfobase.org/oe/abstract.cfm?URI=OPEX-12-19-4353>.
70. E. D. Palik, *Handbook of Optical Constants of Solids* (Academic Press, Boston, 1991).

1. Introduction

With their localized surface plasmon resonance (LSPR) features for enhancing scattering and absorption in a bio-tissue, biocompatible metal nanoparticles (NPs), particularly Au NPs, have found broad biomedical applications, including contrast enhancement in optical imaging [1–10], photothermal therapy [9,11–25], and drug delivery [26–29]. Through a bio-conjugation process, targeted multi-function operation can be implemented [30–35]. For realizing those applications, metal NP distribution in a bio-tissue becomes an important issue. In the cell level, metal NP internalization or expulsion by cells controls the effectiveness of photothermal therapy and drug delivery. In the organ level, the larger-scale metal NP distribution determines the effective coverage of a lesion for diagnosis (imaging) and therapy (heating or drug delivery). Cell uptake and intercellular transport of metal NPs have been widely studied [36–44]. Based on the Brownian diffusion model, the Au NP diffusion coefficient in zebrafish embryos has been estimated [41]. However, from literature survey, the study of metal NP distribution, when they are delivered into a bio-tissue of a larger scale (in the mm range), is quite rare. To develop more effective LSPR-related diagnosis and therapy techniques, investigations of metal NP distribution and their transport process in a bio-tissue sample are needed.

Among various metal NPs used for aforementioned biomedical applications, so far the most commonly used include Au sphere-like NP [45], Au nanoshell [46–48], Au nanorod [49–52], and Au nanocage [5,6,53,54], all of which are fabricated with the techniques of chemical synthesis. Although Ag NPs were also used [41], Au NPs are preferred because of their long-term biocompatibility [55]. However, their LSPR wavelengths are limited to the spectral range shorter than 900 nm in wavelength. Although it is feasible to fabricate Au nanoshells and nanorods for achieving longer LSPR wavelengths, their NP uniformity and fabrication yield become quite low [56,57]. Because of the weaker tissue scattering at a longer wavelength, ~1300 nm in wavelength is an attractive spectral position in bio-photonics application for maximizing light penetration depth in tissue. Beyond this wavelength, water absorption in tissue leads to shallow penetration. Therefore, pushing LSPR wavelength of Au NP into the spectral range of 1300 nm is an important issue for biomedical application. For this purpose, Au nanoring (NR) is a good choice. The fabrication of Au NRs on a substrate has been reported [58–60]. The LSPR wavelength of such an Au NP in water can approach the spectral range of 1300 nm. However, the study of transferring Au NRs from substrate into water solution for biomedical application is still quite rare.

Due to its interference (coherence) detection nature, optical coherence tomography (OCT) is a suitable approach for monitoring the LSPR of Au NPs [61,62]. At LSPR, coherent scattering and absorption of metal NPs are enhanced. Hence, resonant Au NPs can be detected by OCT scanning with high sensitivity. Swept-source OCT systems based on sweeping-

frequency lasers as the light sources around 1300 nm have been widely built for medical diagnosis [63–65]. Besides Doppler OCT, speckle variance OCT represents a powerful tool for monitoring moving subjects in bio-tissue, particularly when the motions of the subjects do not follow a regular pattern like the case of blood flow in microvasculature [66,67]. In speckle variance OCT, by calculating the inter-frame intensity variation of structural images, in which the contrast is based on different time-varying properties of moving subjects versus background tissue components, the general motion information of the moving subjects can be obtained. This approach is suitable for tracking the diffusion of resonant metal NPs in bio-tissue. In this paper, characterizing the LSPR properties of Au NRs and tracking resonant Au NR transport in a bio-tissue with OCT scanning are reported. We first prepare Au NR water solution, in which the LSPR wavelength is longer than 1200 nm such that the LSPR of the delivered Au NRs in a mouse liver sample can enhance backscattering for effective OCT scanning by using an OCT system of 1310 nm in the central wavelength of its light source spectrum. With OCT scanning, the diffusion of Au NRs can be tracked by observing the variation of the average A-mode scan profile and by evaluating the center-of-mass depth of speckle variance distribution at different delay times after a droplet of Au NR solution is applied onto the sample surface. Speckle variance OCT is a useful technique for monitoring irregular object motion in a tissue sample. We use the speckle variance signal to trace the Au NR diffusion in the liver sample and observe systematical diffusion behaviors. The understanding of such behaviors will help us in designing schemes for various Au NP applications.

2. Samples and methods

For fabricating Au NRs on a substrate, we first use a colloidal lithography process through electrostatic adsorption of polystyrene colloidal particles (Duke Scientific Corporation) on a SiO₂ layer of 20 nm in thickness, which is coated on a sapphire substrate with plasma-enhanced chemical vapor deposition [68]. Two samples are prepared with colloidal particle diameters at 150 (sample A) and 100 (sample B) nm. Then, an Au thin film of ~30 nm in thickness is deposited on the top to serve as the source of secondary sputtering, which is implemented with a reactive ion etching (RIE) process. In this process, CHF₃ is used as etchant for forming Au ring structures around the colloidal particles through the mechanism of secondary sputtering. At the same time, the residual Au atoms are removed. Next, an O₂ plasma etching procedure is used to remove the colloidal particles, leaving Au NRs on SiO₂-coated sapphire substrate. Typical scanning electron microscopy (SEM) images of the Au NRs of samples A and B on the SiO₂-coated sapphire substrate are shown in Fig. 1(a) and 1(b), respectively. Here, in samples A and B, the average outer diameters of those Au NRs are about 174 and 118 nm and the inner diameters are 150 and 100 nm, respectively. The average thickness of the NRs in sample A (B) is about 12 (9) nm.

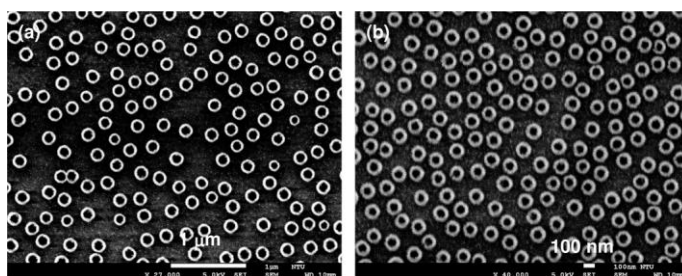


Fig. 1. SEM images of the Au NRs on substrate in samples A (a) and B (b).

The Au NRs are then surface modified by APTS ((3-aminopropyl) trimethoxysilane, 97%, Alfa Aesar) to prevent them from aggregation in water. In this process, a mixture of 1:1 water-ethanol solution (100 mL) is combined with 50 μ L of APTS, and is maintained at pH 10 by adding NH₃ solution. The substrate samples are immersed in this mixture for more than 24

hours and, subsequently, are rinsed with ethanol and dried with N₂ flow. To transfer the substrate-attached Au NRs into water solution, the substrate samples are immersed in a KOH solution (85%, 13.6% w.t. in water) for 15 min to etch the SiO₂ layer between Au NRs and sapphire substrate, followed by a step of gentle rinse with de-ionized water to remove residual KOH. Then, the substrate sample is placed in a glass bottle filled with a proper amount of de-ionized water. After sonication, the Au NRs are transferred into water solution. To avoid the aggregation of Au NRs and hence increase their stability, PEG-Thiol (mPEG-Thiol-5000, Laysan Bio Inc., Arab, AL) is added to the NR solution to make a concentration at 2.5×10^{-5} M. The mixture is then incubated at room temperature for 20 hours. It is noted that APTS is used to avoid aggregation when Au NRs are transferred into water solution. PEG-Thiol is used for maintaining long-term stability of Au NR solution. Figures 2(a) and 2(b) show the close-up SEM images of two and one Au NRs of samples A and B, respectively, after they are lifted off and placed on Si substrates. The images demonstrate that the inner and outer diameters of the NRs change along their ring axes. It is estimated that in an Au NR, the variations of inner and outer diameters can be as large 40% from the individual maximum values in either sample.

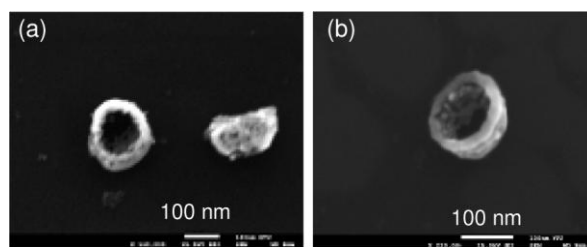


Fig. 2. Close-up SEM images of the Au NRs after liftoff in samples A (a) and B (b).

In OCT scanning experiments, a swept-source OCT system is used. In this system, a sweeping-frequency laser source with the output spectral peak at 1310 nm (the spectrum is shown in Fig. 3) is used as the light source. The light source is connected to a Mach-Zehnder interferometer, which consists of two optical couplers and two circulators. The interference fringe signal is detected by a balanced photo-detector and sampled by a high-speed digitizer. The achieved system sensitivity and axial resolution in tissue are 103 dB and 6 μ m (in tissues) at the depth of 1 mm, respectively. It takes about 0.1 s to complete a two-dimensional image of 1.3 mm in lateral dimension. The detailed descriptions about the OCT system and operation can be found in Refs. [63–65]. It is noted that for obtaining an OCT image in this paper, we first make 1950 A-mode scans in the lateral range of 1.3 mm with one scan every 0.67 μ m. To reduce the background noise, we take the average of three adjacent A-mode scans for composing an OCT image. Therefore, there are 650 A-mode scans with one scan every 2.01 μ m in one image. Since all the samples are scanned under the same OCT operation conditions, the variation of absolute OCT signal intensity from one image to another must be small. The pixel size in an OCT image is about 7 μ m (depth) x 5 μ m (width).

For demonstrating the transport of delivered Au NRs in tissue, we choose mouse liver as sample because of its structure uniformity (suitable for the first-stage study), our capability of keeping the sample fresh for making the condition close to *in vivo* experiment, and the biomedical importance in understanding NP migration behavior in liver. A male C57/black mouse, 7–8 weeks old, fed chow and water ad libitum under standard light-dark cycle conditions was subjected to simple laparotomy by midline incision after cervical translocation. The five liver lobes of the mouse were resected and rinsed briefly with Ringer's solution, then all vasculature were sealed immediately using sterile hydroactive gel (Convatec, New Jersey). The liver lobes were kept under 100% humidified air at room temperature, and their visceral peritonea were torn apart from falsiform ligament to expose the hepatic tissue before application of Au NR solution. For OCT scanning, a solution droplet of Au NRs (about 3 μ L) is applied to the surface of a mouse liver sample. An OCT image of 1.3 mm in lateral

dimension is acquired before the application of the solution droplet for comparing with the results after Au NR delivery. After the application of the solution droplet, an OCT image is obtained every 10 sec for 60 min at the same location.

3. Localized surface plasmon properties of Au nanorings

The estimation of Au NR concentration in water solution starts with the calculation of the total Au NR number on the substrate based on the SEM observation [68]. The NR concentrations in the solutions of samples A and B are estimated to be 1.09×10^9 and $2.01 \times 10^9 \text{ cm}^{-3}$, respectively, by assuming that 40% NRs are lost in the process of transferring NRs into water solution. The water solutions of the two samples are then condensed with centrifugation under the condition of 5000 rpm for 40 min by a factor of about 27 to give the final concentrations of 2.94×10^{10} and $5.43 \times 10^{10} \text{ cm}^{-3}$ in samples A and B, respectively. These values are essentially consistent with the concentration estimates from the measurement of inductively coupled plasma mass spectrometry, which results in 2.40×10^{10} and $8.03 \times 10^{10} \text{ cm}^{-3}$ for samples A and B, respectively. It is noted that with the aforementioned concentrations, the average distances between two neighboring Au NRs are $\sim 3 \mu\text{m}$ in sample A and $\sim 2.5 \mu\text{m}$ in sample B. In such a solution, the LSPR coupling between neighboring Au NRs must be weak. Optical transmission of the water solutions of Au NRs are measured with a UV-vis spectrophotometer (Jasco V-570) to show the spectral variations of extinction cross sections of the two samples in Fig. 3 (the left ordinate). The extinction cross sections are obtained by dividing the measured extinction coefficients by the Au NR concentrations given above. Here, one can see the major peaks of extinction, corresponding to the LSP dipole resonances in water, at 1240 and 1030 nm for samples A and B, respectively. In this figure, the spectrum of the sweeping-frequency laser source of the used OCT system is also shown for comparison (the right ordinate). The light source spectrum with its peak at 1310 nm and spectral full-width at half-maximum at $\sim 100 \text{ nm}$ is covered by the long-wavelength side of the LSP dipole resonance range of sample A. However, the LSP dipole resonance range of sample B is quite far away from the OCT light source spectrum. The secondary peaks of the extinction spectra in Fig. 3 correspond to the mixture of the higher-order resonance across the ring and the resonance along the ring axis. It is expected that the LSP dipole resonance peak red shifts and overlaps better with the OCT light source spectrum when the Au NRs are delivered into tissue, which has a higher refractive index of ~ 1.4 . From Fig. 3, one can see that the extinction cross sections of sample A (B) at the individual LSPR wavelength and 1310 nm are 5.56×10^{-10} and $5.22 \times 10^{-10} \text{ cm}^2$ (2.84×10^{-10} and $1.21 \times 10^{-10} \text{ cm}^2$), respectively. Those numbers are also shown in Table 1 for comparing with the corresponding values from other methods later.

To confirm the level of Au NR extinction cross section, we place a droplet of Au NR solution on a coverslip for OCT scanning. Figures 4(a) and 4(b) show the OCT scanning images of samples A and B, respectively. Because the lateral scanning is implemented by the swing of a galvanometer, the image surfaces show slightly concave geometries. The stronger and weaker OCT signal intensities from the solution droplets in Figs. 4(a) and 4(b), respectively, indicate the different scattering cross sections at 1310 nm between samples A and B. By averaging all the A-mode scan profiles of the OCT images in Figs. 4(a) and 4(b) and then multiplying a fixed-focus effect function, f , of [69]

$$f = \sqrt{\left(\frac{z - z_{cf}}{z_R}\right)^2 + 1}, \quad (1)$$

where z is the depth, z_{cf} is the depth of the focal point, and z_R is the Rayleigh length, which is equal to the field of view and is around $154 \mu\text{m}$, we can plot the two curves in Fig. 5 for demonstrating the decay profiles of samples A and B. It is noted that in averaging the A-mode scan profiles, the sample surface points are aligned with each other. In Fig. 5, one can see that in samples A and B, when the depths are smaller than 125 and $150 \mu\text{m}$, respectively, the curves in the semi-log scale show linear variations, from which extinction coefficients can be

calibrated by least-square fitting the two curves with straight lines. The calibrated extinction coefficients are 14.30 and 5.83 cm^{-1} for samples A and B, respectively. The Au NR extinction cross section can be obtained from the extinction coefficient divided by the Au NR concentration. By using the aforementioned estimated Au NR concentrations, we can obtain 4.86×10^{-10} and $1.07 \times 10^{-11} \text{ cm}^2$ for the extinction cross sections of samples A and B, respectively, at 1310 nm . These values are reasonably consistent with those calibrated from transmission measurement at the same wavelengths, which are 5.22×10^{-10} and $1.21 \times 10^{-10} \text{ cm}^2$ for samples A and B, respectively (see Table 1). The average OCT intensity profiles in the deeper portions shown in Fig. 5 are not consistent with the straight-slope trends of the shallower portions. The enhanced OCT intensities, with respect to the straight-slope trends, in the deeper portions can be attributed to the sedimentation of Au NRs in the solution droplets. However, the sedimentary Au NRs do not directly contact the coverslip. They are still suspended in the deeper portions of the solution droplets. In this situation, the deeper portions have higher NR concentrations than those in the shallower portions. Hence, the extinction cross section evaluations based on the overall average NR concentrations of the droplets can be underestimated.

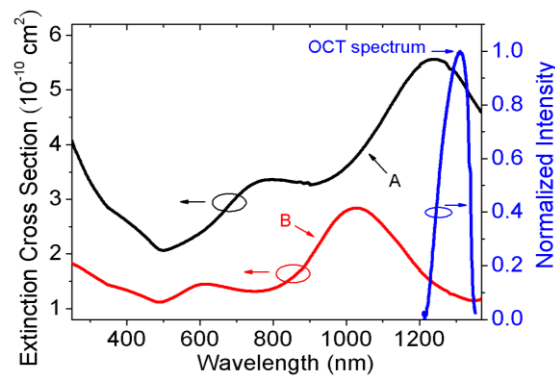


Fig. 3. Spectral variations of extinction cross sections of the NRs in water in the two samples obtained from optical transmission measurement.

Table 1. Extinction cross sections of samples A and B obtained from different methods, including transmission, OCT scanning, and simulation

$\times 10^{-10} \text{ cm}^2$	Sample A		Sample B	
	Resonance wavelength (1240 nm)	1310 nm	Resonance wavelength (1030 nm)	1310 nm
Transmission	5.56	5.22	2.84	1.21
OCT scanning	—	4.86	—	1.07
Simulation	31.1	23.9	16.9	1.3

To further understand the resonance behaviors of the fabricated Au NRs, numerical simulations based on the finite-element method are performed. In our simulation, the resonance behaviors of the Au NRs are obtained with the excitation light incident along the ring axis. In Fig. 6, the extinction, scattering, and absorption cross sections as functions of wavelength of the two samples with ambient refractive index at 1.33 corresponding to the situation of an NR in water are shown. The used NR parameters include the outer diameter at 179 (120) nm, inner diameter at 149 (97) nm, and height at 95 (60) nm for sample A (B). For simulations, the dispersive dielectric constant of Au follows the experimental data in Ref. [70]. In Fig. 6, one can see that scattering is stronger than absorption around the resonance wavelength in either sample A or B. In OCT scanning, the enhanced backscattering can be due to either the LSPR-enhanced scattering or absorption of Au NRs. With enhanced absorption of

Au NRs, the heating effect of the surrounding medium can change local refractive index such that local backscattering is enhanced.

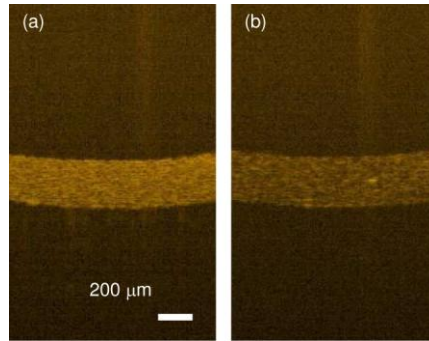


Fig. 4. OCT images of Au NR solution droplets on coverslip in samples A (a) and B (b).

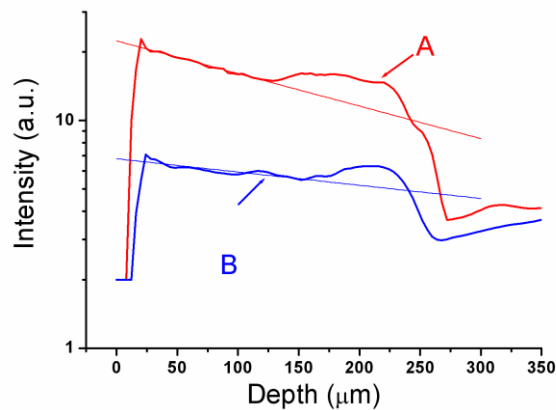


Fig. 5. Average A-mode scan profiles multiplied by a fixed-focus effect function of the two samples.

The extinction cross sections of samples A and B at their individual LSPR wavelengths and at 1310 nm are shown in the row of simulation in Table 1. In this table, we compare the results of the extinction cross sections of the two samples from three methods, including optical transmission measurement, OCT scanning, and simulation. Here, one can see that the extinction cross sections at 1310 nm obtained from OCT scanning and transmission measurement are quite consistent. The slightly lower values from OCT scanning can be attributed to the overestimated NR concentrations in the shallower portions of Fig. 5, in which the OCT signals are used for calibrating the extinction cross sections. Except that of sample B at 1310 nm, the simulation results are significantly larger than those from transmission measurement. At individual resonance wavelengths, the simulation results are 5.6-6 times those from transmission measurement for both samples. It is noted that the simulation results are obtained under the assumption of optimized excitation of LSPR in a single NR and hence represent the case of perfectly aligned Au NR distribution of negligible mutual coupling. The significantly smaller extinction cross sections from experiments can be attributed to the following four factors. First, due to the random orientation distribution of Au NRs in water, the average extinction cross section drops by a certain percentage. Second, because of the non-uniform distribution of Au NR geometry, the LSPR spectrum is broadened. In this situation, the peak level at the LSPR wavelength is reduced and the spectral wing levels, particularly the tails, are enhanced. Therefore, as shown in Table 1, at 1310 nm, the simulation results are larger than those from transmission measurement by only 4.6 and 1.07 times in samples A and B, respectively. The third factor is related to the changing ring diameter along its axis in a

fabricated Au NR. This factor also broadens the LSPR spectrum. Finally, the Au NR concentrations can be overestimated such that the experimentally calibrated extinction cross sections are underestimated.

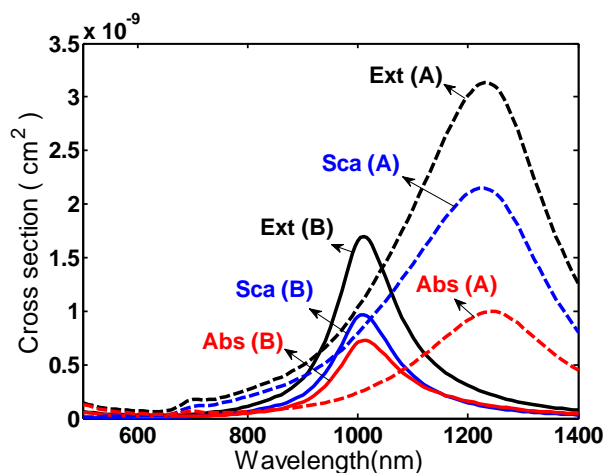


Fig. 6. Simulation results of the extinction (Ext), scattering (Sca), and absorption (Abs) cross sections as functions of wavelength of a single Au NR of samples A and B. The LSPR is excited with a plane wave incident along the ring axis.

4. OCT scanning results of mouse liver samples with delivered Au nanorings

Figures 7(a)–7(d) show the OCT images of a mouse liver sample before, 0, 30, and 60 min after the application of an Au NR solution droplet of sample A. In Fig. 7(b), one can see the image of the solution droplet with strong backscattering of resonant Au NRs. Within the mouse liver sample, a brighter stripe at the depth between 400 and 600 μm can be seen in each figure that is irrelevant to Au NR delivery. The depth of the brighter stripe corresponds to the location of the focal point of the used objectives for focusing light into the sample in OCT scanning. The sample depth of the focal point may vary from sample to sample because of their different sizes. To observe the transport of Au NRs in the liver sample, we evaluate the variance of OCT signal intensity at each image pixel based on four successive OCT images (10 sec separation between two successive images) to form the speckle variance images in Fig. 8 [66,67]. Figures 8(a)–8(e) show the speckle variance images in the liver sample at 15, 22.5, 30, 45, and 60 min after the application of the Au NR solution droplet (sample A). For clearly demonstrating the speckle variance distributions in Figs. 8(d) and 8(e), the signal intensities in these two figures have been numerically enhanced by 50 times. The intensity distributions in Figs. 8(a)–8(e) are related to the motion speed of Au NR diffusion. We can only show such images taken after the solution droplet is completely diffused into the liver sample (~ 15 min later) because the solution droplet on the sample surface distorts the images and leads to artifacts in evaluating the speckle variance. From Figs. 8(a)–8(e), one can see that the distribution of high speckle variance moves to deeper sample layers with time. Although the stronger OCT signal intensity near the focal point may result in a higher variance level, the observation of the speckle variance variation is not affected by the focal point issue, as to be demonstrated later. To provide a more complete picture of resonant Au NR diffusion in the mouse liver sample, Media 1 shows the motion pictures of OCT scanning for 60 min starting at the application of the solution droplet. Media 2 shows the motion pictures of speckle variance mapping for 45 min starting at the time of complete diffusion of the solution droplet into the liver sample.

On the other hand, when a solution droplet of sample B is applied to a liver sample, the weak LSPR leads to quite different results, as demonstrated in Fig. 9. In this case, although the Au NRs in the solution droplet can also produce observable backscattering in OCT scanning,

as shown in Fig. 9(b), the signal intensity is significantly weaker than that in Fig. 7(b). The bright spot in Fig. 9(b) is an artifact caused by the surface reflection of the solution droplet. With sample B, Au NRs are expected to also diffuse into the mouse liver sample. However, due to the weak LSPR of this sample at 1310 nm, we can hardly observe any change in OCT scanning images after the Au NRs are delivered into the liver sample, as shown in Figs. 9(a)–9(d), which show the images taken before, 0, 30, and 60 min after the application of the solution droplet, respectively. Meanwhile, little information can be obtained from the speckle variance analysis of the OCT scanning images, as demonstrated in Figs. 10(a)–10(c), in which the speckle variance images in the liver sample at 15, 22.5, and 30 min, respectively, after the application of the Au NR solution droplet are shown. It is noted that to clearly demonstrate the images in Figs. 10(a)–10(c), the speckle variance signal strengths in these images are numerically enhanced by four times. In our experiment, because sample B has a higher Au NR concentration than that of sample A, the overall weaker LSPR behavior in sample B must be due to its weaker LSPR of an individual Au NR. We also repeated the OCT scanning on a mouse liver sample by applying a droplet of pure water. In this situation, the scanning results are similar to those in the case of non-resonant Au NR delivery.

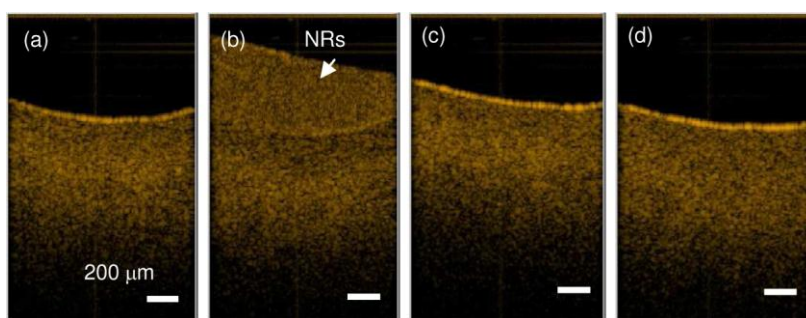


Fig. 7. (Media 1) OCT images of a mouse liver sample taken before (a), 0 (b), 30 (c), and 60 min (d) after the application of an Au NR solution droplet of sample A onto the sample surface.

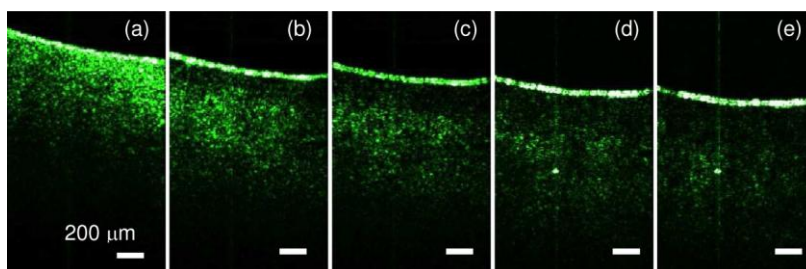


Fig. 8. (Media 2) Speckle variance images of the mouse liver sample including Au NRs of sample A, evaluated based on the OCT images, at 15 (a), 22.5 (b), 30 (c), 45 (d), and 60 (e) min after the application of an Au NR solution droplet. To clearly demonstrate the images in parts (d) and (e), the speckle variance signal strengths in these two images are numerically enhanced by 50 times.

From Figs. 7–10 and Media 1 and Media 2, one can see that the sample surface level drops with delay time after the solution droplet is completely diffused into a sample. This behavior is particularly clear in the early stage of OCT scanning. It is due to sample shrinkage during OCT scanning, particularly in the upper portion of the sample, caused by sample dry up and water diffusion into deeper layers. The shrinkage range can be estimated by tracking the distance between the image top end and the sample surface at the center in the lateral dimension of an image as a function of delay time. This distance as a function of delay time in the experiment with sample A is shown in the red curve (with the left ordinate) and the fitting curve with a fifth-order polynomial (the black dashed curve) in Fig. 11. By taking the derivative of the fitting curve, we can obtain the sample shrinkage speed, as shown in the blue

curve (with the right ordinate) of Fig. 11. It is noted that when the delay time is larger than 25 min, the sample shrinkage speed becomes lower than 7.5 $\mu\text{m}/\text{min}$. In this situation, within 40 sec, over which a data point of speckle variance is evaluated, the sample shrinkage range is smaller than 5 μm . This range is smaller than the depth pixel size of 7 μm . In other words, between 15 and 25 min in delay time, the observed speckle variance signals can be mainly caused by sample shrinkage. However, beyond 25 min in delay time, the observed speckle variance signals are essentially due to Au NR diffusion.

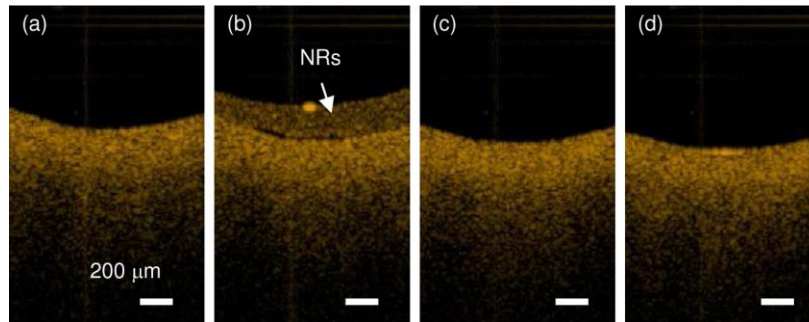


Fig. 9. OCT images of a mouse liver sample taken before (a), 0 (b), 30 (c), and 60 min (d) after the application of an Au NR solution droplet of sample B onto the sample surface.

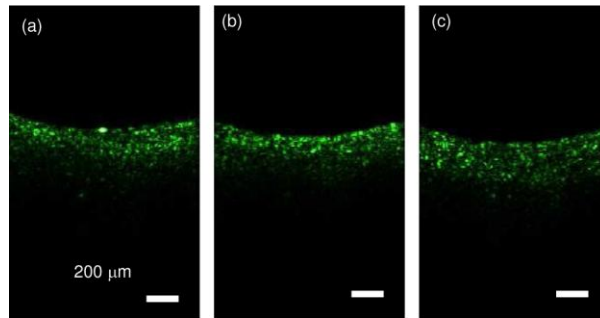


Fig. 10. Speckle variance images of the mouse liver sample including Au NRs of sample B, evaluated based on the images in Fig. 9, at 15 (a), 22.5 (b), and 30 (c) min after the application of an Au NR solution droplet. To clearly demonstrate the images, the speckle variance signal strengths in these images are numerically enhanced by four times.

To further understand the Au NR diffusion behavior in the mouse liver sample, we take the average of all the A-mode scan profiles in the OCT image taken at a particular time and plot the result in Fig. 12. Before the average, the sample surface points of all the A-mode scan profiles are aligned with each other. In Fig. 12, we show the average A-mode scan profiles (thick curves) before, 20, 30, and 60 min after the application of the solution droplet of sample A for comparison. Here, for reasonable comparison, the surface points of the average A-mode profiles at different delay times are also aligned with each other. In Fig. 12, the peaks between 100 and 150 μm in depth are caused by sample surface scattering. Here, one can see that surface scattering strength increases with delay time. This phenomenon is caused by the accumulation of Au NRs (with water) on the sample surface. Through continuous OCT light illumination, the surface Au NR solution is gradually dried up and condensed such that the surface scattering becomes stronger and stronger with delay time. This phenomenon can also be clearly seen in Figs. 7(c) and 7(d). The surface speckle variance signals shown in Figs. 8(b) and 8(c) are caused by the sample shrinkage process during OCT scanning. Surface accumulation of Au NRs should also occur in the case of sample B. However, because the non-resonant Au NRs cannot be clearly seen with OCT scanning, we cannot observe enhanced surface scattering effect in Fig. 9(c), 9(d), 10(b), or 10(c). By comparing the average profiles

beyond 150 μm in depth at different delay times after the droplet application, one can see that the profile peak generally shifts to larger depths with increasing delay time. To more clearly compare the variation trend of the average A-mode profile beyond 150 μm in depth, they are fitted with second-order polynomials, which are plotted as the smooth thin curves in Fig. 12. Based on the fittings, one can see that at 20, 30, and 60 min in delay time, the profile peaks are located at 314, 414, and 472 μm in depth (with respect to the individual sample surfaces), respectively. Such a trend cannot be caused by sample shrinkage, which should lead to reduced profile peak depth if the peak is produced by certain feature other than diffused Au NRs, such as the focal point or a tissue structure of strong backscattering. This trend clearly demonstrates the diffusion of Au NRs into the liver sample to reach a deeper layer after a longer transport time. It is noted that beyond 150 μm in depth, the dot-dashed curve, which describes the condition before droplet application, has a maximum around 450 μm in depth. This depth roughly corresponds to the focal point of OCT light illumination. The depth of focal point around 450 μm may affect the determination of the Au NR diffusion range, particularly in the case of 60 min in delay time. With the LSPR of the delivered Au NRs, the OCT signal intensity is expected to become stronger. However, in Fig. 12, the profile level of the curve representing the condition before the droplet application (the dot-dashed curve) beyond 150 μm in depth is comparable to those after the droplet application. This result is attributed to the significantly weaker surface backscattering in the case before droplet application. If the surface scattering strengths of all those cases in Fig. 12 were the same, the OCT signal intensity level beyond 150 μm in the case before droplet application would be lower than those of droplet application.

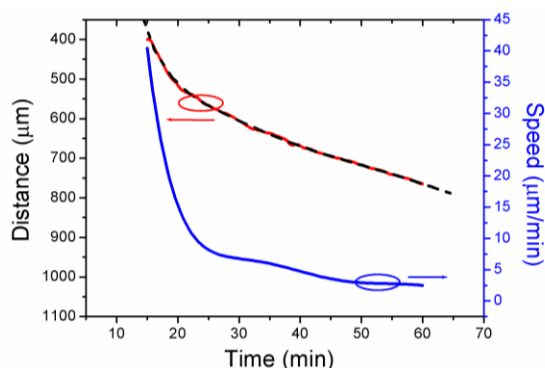


Fig. 11. Distance between the image top end and the sample surface at the center in the lateral dimension of an image as a function of delay time in the experiment with sample A (the red curve) and the fitting with a fifth-order polynomial (the black dashed curve) in the left ordinate. Sample shrinkage speed is also shown in the blue curve (in the right ordinate).

As mentioned earlier, the distribution of high speckle variance level shifts to a deeper layer with delay time. For demonstrating this trend more clearly, we evaluate the center-of-mass depth of the speckle variance distribution as a function of delay time (starting at 25 min in delay time) to plot the curves in Fig. 13 for the cases of samples A and B. For comparison, the result in the case of applying a pure water droplet onto a liver sample is also shown. It is noted that the zero level of the center-of-mass depth is set at the individual sample surface at each delay time such that the sample shrinkage factor can be essentially removed. The thin lines in Fig. 13 represent the least-square fitting slopes of the data of center-of-mass depth. Because in the cases of water and sample B, the delivered substances do not significantly change the OCT scanning images, we cannot observe any major feature except a slightly increasing trend in the curves of center-of-mass depth. With resonant Au NRs, the curve of sample A in Fig. 13 clearly shows an increasing slope of 6.40 $\mu\text{m}/\text{min}$. Because the center-of-mass depth of speckle variance represents the location of major NR transport, the slope of 6.40 $\mu\text{m}/\text{min}$ can be regarded as the migration speed of Au NRs in mouse liver in the diffusion process (starting at 25 min after the NR solution application). From the speckle variance images, one can also

observe that the distribution of high speckle variance level becomes broader as delay time increases. Figure 14 shows the depth standard deviations of speckle variance in the three cases of Fig. 13. Again, the thin straight lines here represent the least-square fitting results. In the cases of sample B and water, only slightly decreasing trends are seen. The clear increasing trend with a slope of $7.55 \mu\text{m}/\text{min}$ in the case of sample A indicates the broadening process of moving NR distribution with delay time in the mouse liver sample.

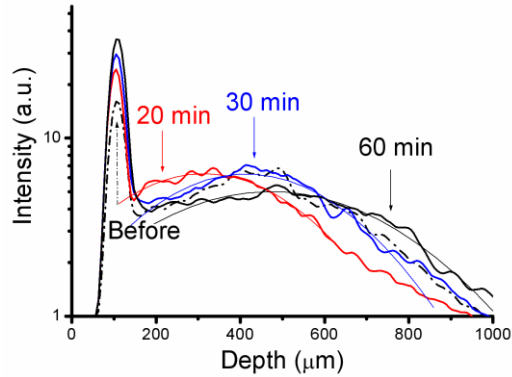


Fig. 12. Average A-mode scan profiles (thick curves) of the OCT images taken before, 20, 30, and 60 min after the application of an Au NR solution droplet of sample A. The second-order polynomial thin curves are used to fit the average A-mode scan profiles for finding the depths of maximum intensities for the cases of 20, 30, and 60 min in delay time.

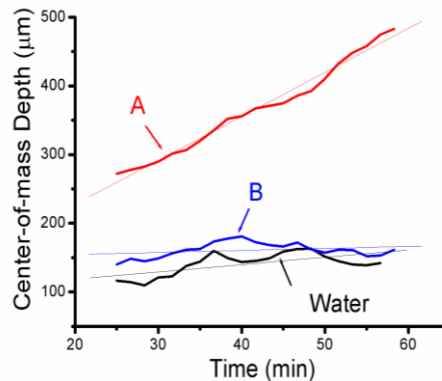


Fig. 13. Center-of-mass depths of speckle variance distributions in the cases of samples A and B, and water delivery as functions of delay time.

It is noted that besides Au NR diffusion, the evaluations of the center-of-mass depths and depth standard deviations of speckle variance distributions can be affected by other factors, such as the focusing of the illumination light beam. However, because the samples in the three cases of resonant Au NR, non-resonant Au NR, and water applications are scanned under the same OCT operation conditions, the effects of other factors should be common among the three cases. The observed different results between the three cases must be caused by the different LSPR behaviors of diffused Au NRs. Because OCT scanning monitors the refractive index variation in the sample, the recorded OCT signals can be due to the LSPR-enhanced scattering of Au NRs. They can also be due to the refractive index change resulting from local heating, which is caused by LSPR-enhanced absorption of Au NRs. However, it is difficult to determine the dominating factor.

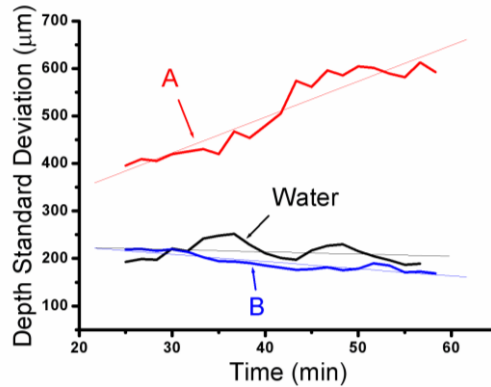


Fig. 14. Depth standard deviation of speckle variance distributions in the cases of samples A and B, and water delivery as functions of delay time.

5. Conclusions

In summary, we have demonstrated the preparation of water solutions of Au NRs with different LSPR wavelengths. The LSPR-induced extinction cross sections at 1310 nm were estimated with OCT scanning of solution droplets on coverslip. The results were reasonably consistent with the data at individual LSPR wavelengths and at 1310 nm obtained from transmission measurements and numerical simulations. The resonant and non-resonant Au NRs were then delivered into mouse liver samples for tracking Au NR diffusion in the samples through continuous OCT scanning. With resonant Au NRs, the average A-mode scan profiles of OCT scanning at different delay times clearly showed the extension of strong backscattering depth. The calculation of speckle variance among successive OCT scanning images, which could be used to represent the local transport speed of Au NRs, led to the demonstrations of downward propagation and spreading of major Au NR motion spot with time. In one of the future efforts, Au NR of a smaller diameter with its LSPR wavelength in tissue being maintained close to 1300 nm will be designed and fabricated. Such a structure can be implemented by decreasing the ring thickness when the ring diameter is reduced.

Acknowledgement

This research was supported by National Science Council, The Republic of China, under the grants of NSC 98-2622-E-002-002-CC1, NSC 98-2218-E-002-036, NSC 98-2221-E-002-033, by National Health Research Institute, The Republic of China, under the grant of NHRI-EX98-9616EI, a by the Excellent Research Projects of National Taiwan University (98R0061-04 and 98R0062-07), and by US Air Force Scientific Research Office under the contracts of AOARD-07-4010 and AOARD-09-4117.